IEEE Access
Multidisciplinary | Rapid Review | Open Access Journal

Received 11 January 2026, accepted 2 February 2026, date of publication 6 February 2026, date of current version 11 February 2026.

Digital Object Identifier 10.1109/ACCESS.2026.3662089

RESEARCH ARTICLE

Two Modulation Techniques for WPT Systems

MANUELE BERTOLUZZO, NICOLA BIANCHI, (Fellow, IEEE), AND FRANCESCO TRIPALDI
Department of Industrial Engineering, University of Padova, 35131 Padua, Italy
Corresponding author: Manuele Bertoluzzo (manuele.bertoluzzo@unipd.it)

ABSTRACT Wireless power transfer technology is widely studied for applications related to recharging of the batteries of electric vehicles, but also finds applications in air, marine and medical sectors. A common feature of the different implementations of the wireless power transfer is a transmitting coil supplied by a two-leg high-frequency inverter. Different modulation techniques have been proposed for the generation of the switching commands of the inverter, aimed at enhancing the output voltage control or the overall system efficiency. In any case, only one control variable is in charge of generating the commands for both the legs of the inverter. This paper proposes two modulation techniques that use two independent control variables to control the two inverter legs. No relation is imposed between the control variables and, for any possible combination of them, the switching behavior of the inverter and the harmonic content of the generated voltage are analyzed. It is then recognized that some combinations of the control variables, which define the inverter control strategies, achieve better efficiency performance, especially when operating in low power conditions, than the conventional phase shift technique, usually applied in the wireless power transfer systems. This feature makes the proposed approach particularly suitable for both static and dynamic wireless power transfer systems, where coupling conditions and load may vary over a wide operating range so that different presented control strategies can be profitably applied. The presented modulation techniques are implemented in a prototypal system and experimented under different operating conditions. Consistently with the theoretical analysis, experiments demonstrated that the proposed modulation techniques enable an even distribution of the switching voltage solicitations between the two legs of the inverter and achieve higher efficiency. With respect to the conventional phase shift modulation technique, depending on the used modulation technique and the considered power range, the improvement of the overall system efficiency was as high as 10% whilst the improvement of the inverter efficiency reached 20%.

INDEX TERMS Harmonic analysis, pulse width modulation, voltage source inverters, wireless power transfer.

I. INTRODUCTION

Wireless Power Transfer (WPT) technology is a promising solution to free the user of an electric vehicle from the hassle of having to fiddle with plugs and cables when the vehicle's battery needs to be recharged [1]. The same technology, applied to running vehicles, could solve the concerns arising from the long recharge time of the batteries, their size, weight and cost, and the availability of recharging stations [2]. In addition to land vehicles, the WPT technology also finds application in the air [3], [4], marine [5], and medical sectors [6].

The associate editor coordinating the review of this manuscript and approving it for publication was Riccardo Mandrioli.

The core of the inductive WPT technology, the only applied to the battery charging of electric vehicles, is a pair of coupled coils, with the transmitting coil supplied by a two-legs high frequency inverter (HFI). The frequency of the supply voltage and current of WPT systems (WPTSs) is much higher than those of other widespread applications of static power converters, such as motor driving or electric power generation or distribution. Indeed, the rules specify that the transmitting coil of an inductive WPTS should be supplied at a frequency around 85 kHz [7]. The rules, however, do not specify which kind of modulation should be adopted. In WPTS, the conventional pulse width modulation is not applied because its adoption would require switching the HFI at very high frequency, thus increasing its losses. Instead, different

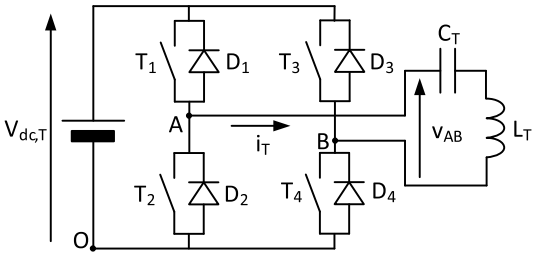

FIGURE 1. Schematic of the transmitting section of a WPT system.

techniques are used to maintain the switching frequency of the HFI equal to the transmitting coil supply frequency [8]. Among these techniques, the phase shift technique (PST) is widely adopted due to its simple implementation and its ability to generate an alternating voltage in ideal conditions. To maintain the zero-voltage switching (ZVS) in a wider range of operation, other techniques such as asymmetrical clamped mode [9] can be used, but at the cost of generating a voltage with a direct component. The direct component is avoided if the pulse density modulation is used [10], but it causes large oscillations of the output current amplitude. These oscillations are mitigated in the enhanced pulse density modulation [11]. The latter two techniques, as well as [12] and [13], do not allow for continuous control of the output voltage as they are based on an on-off application of the switching commands during a whole power supply period. Consequently, the required output voltage is obtained as the average voltage over several supply periods, whereas the PST and the asymmetrical clamped mode, which operate on the duty cycle of the generated waveforms, allow for applying the required voltage within a single period.

The manipulation of a single variable to control both legs of the HFI is a characteristic feature of many modulation techniques used in WPT. Some proposals to use two control variables have been made [14], [15], but they consider an HFI with two outputs, so from this point of view there is no fundamental difference from the conventional PST. Other approaches, based on PST, are applied to WPTSs where the receiver section is equipped with an active rectifier [16], [17].

This paper presents two modulation techniques derived from the PST, whose performance is considered as a reference, and which are capable of performing a continuous regulation of the generated voltage, and, moreover, are characterized by the feature of manipulating two control variables, one for each leg of the HFI. Exploiting two degrees of freedom instead of only one, the proposed modulation techniques offer higher flexibility than the PST. For example, one of them can reproduce the same waveforms generated by the PST, but with a better distribution of the solicitations among the switches, and allows increasing significantly the efficiency of the HFI when it operates at low power by commutating only the switches of one HFI leg. The other technique is optimized for the low power operations and the switching at half of the nominal frequency. At even lower power levels, both the proposed techniques can operate by switching only one leg of the HFI to further increase its efficiency and, consequently, the efficiency of the overall WPTS.

The paper analyzes in detail the performance of the two modulation techniques from the point of view of the solicitations sustained by the commutating switches and of the harmonic content of the generated voltages. The proposed modulation techniques have been implemented in the experimental WPTS described in [18]. Some experimental tests have been performed on the prototype to confirm the feasibility of the two modulation techniques and to compare their efficiency performance during the power transfer operations.

Section II of the paper briefly presents the proposed techniques and the PST, used as a reference. Section III describes the conventional PST, analyzes the commutation of the switches and the harmonic contents of the generated voltage. Section IV analyzes the first of the proposed techniques. It is demonstrated that the commutations happen in the same way as in PST but with an even distribution of the solicitations among the two HFI legs. The harmonic content of the generated voltage is analyzed as a function of the two control variables, i.e. the two duty cycles, and represented with the help of maps. Section V analyzes in the same way the second of the proposed techniques. Section VI explains how the HFI control algorithm could take advantage of the two degrees of freedom offered by proposed techniques. Some examples are given that show how different strategies can be implemented to replicate the same behavior of the PST but with a better sharing of the voltage solicitations and higher efficiency. Section VII reports the experimental results obtained from a prototypal WPTS and compares the performance of the control strategies that use the proposed modulation techniques with the performance of the PST. Section VIII gives a hint about a possible management of the different strategies in order to maintain the maximum efficiency of the HFI in any working condition. Section IX concludes the paper.

II. PROPOSED COMMUTATION TECHNIQUES

The transmitting section of a WPTS has the simplified scheme sketched in Fig. 1. The dc side of the HFI is supplied by the constant $V_{dc,T}$ voltage. On its turn, the HFI supplies the set formed by the transmitting coil, denoted by its self-inductance L_T, and the resonant compensation network, which in this case has a series topology and consists of the capacitor C_T. In order to avoid short circuits of the HFI legs, the commutations of T_1 and T_3 entail complementary commutations of T_2 and T_4. The latter ones lead or lag the commutations of the switches T_1 and T_3 to implement the dead time.

A. PHASE SHIFT TECHNIQUE

Usually, the HFI is controlled using the PST. It is implemented by commanding the two legs of the HFI in order to generate two square-wave voltages v_{AO} and v_{BO} with 50% duty cycle and with the same frequency f_N as the required

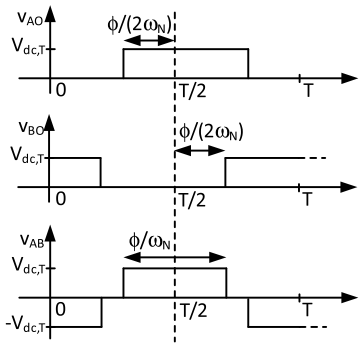

FIGURE 2. Waveforms obtained with the PST.

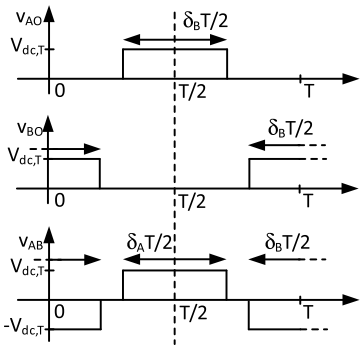

FIGURE 3. Waveforms obtained with the anti-PT.

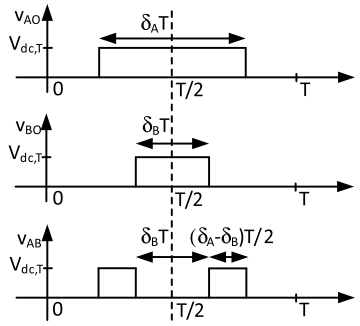

FIGURE 4. Waveforms obtained with the in-PT.

supply voltage v_{AB}. The amplitude $V_{AB,fN}$ of the 1st harmonic of v_{AB} is controlled by adjusting the phase shift ϕ between the phase voltages v_{AO} and v_{BO}. The phase shift is the only control variable of the PST and is symmetrically shared by leading v_{AO} and lagging v_{BO}, so that the phase $\phi_{AB,fN}$ of the 1st harmonic of v_{AB} is unaffected by ϕ.

The actual waveforms of v_{AO}, v_{BO}, and v_{AB} are drawn in Fig. 2, where ω_N and T denote the supply angular frequency and the relevant supply period.

B. ANTI-PHASE TECHNIQUE

The first different approach to the generation of v_{AB} proposed in this paper consists of commanding the HFI to obtain two phase voltages v_{AO} and v_{BO} with a fixed phase and variable duty cycle. This solution, which can be considered somewhat dual to the PST, originates the waveforms reported in Fig. 3. The figure shows that the 1st harmonics of v_{AO} and v_{BO} are in phase opposition to each other. For this reason, this modulation technique is denoted as anti-phase technique (anti-PT). The control variables used in the anti-PT are δ_A and δ_B, i.e. the duty cycles of the command signals of the upper switches T_1 and T_3 of the legs A and B of the HFI.

C. IN-PHASE TECHNIQUE

Like the anti-PT, the second modulation technique proposed in this paper commands the HFI to obtain phase voltages with a fixed phase and variable duty cycle. However, as defined by its denomination, the in-phase technique (in-PT) imposes that the 1st harmonics of voltages v_{AO} and v_{BO} are in phase each to the other instead of being in phase opposition. Also in this case, the two control variables are the duty cycles δ_A and δ_B. As shown in Fig. 4, the voltage v_{AB} exhibits two pulses during each supply period. Both of them are positive if $\delta_A > \delta_B$, otherwise they are negative.

III. PHASE SHIFT TECHNIQUE ANALYSIS

Figure 5, obtained from inspection of Fig. 2, highlights the commutation instants of the upper switches T_1 and T_3. Because of the dead times, the lower switch T_4 is switched on after switching off T_3, the lower switch T_2 is switched off before switching on T_1, T_4 is switched off before switching on T_3, and T_2 is switched on after switching off T_1. In the following analysis, no hypotheses are made about the waveform of the current i_T, other than that it is positive when the commutations denoted as $T_{1,ON}$ and $T_{3,ON}$ occur, and negative in correspondence with the other two commutations. In order to simplify the drawing, a nearly sinusoidal current has been represented in Fig. 5.

A. COMMUTATIONS

Depending on the sign of the supply current i_T, the switches and the freewheeling diodes exhibit different behaviors during the dead times. With the help of Figs. 1 and 5, it can be recognized that when T_3 is switched off, the negative current i_T starts flowing through the freewheeling diode D_4, thus the voltage across T_4 is very low when it is switched on after the expiration of the dead time so that a ZVS commutation happens, as is reported in the top-right cell of Tab. 1. The following commutation is relevant to the pair T_1, T_2. T_2 is switched off while i_T is positive and the current starts flowing through the diode D_2 before T_1 is switched on. In this case T_1 is switched on while the voltage across it is about equal to $V_{dc,T}$ and, hence, it is subjected to higher solicitation than T_4. For this reason, this commutation is marked as a high voltage switching (HVS) in Fig. 5 and in the bottom-left cell of Tab. 1. The subsequent switching on of T_3 occurs with a positive i_T while D_3 is already conducting, and hence it is a ZVS commutation. The last commutation of T_1 is followed by the switching on of T_2 while i_T is negative and D_1 is conducting. Hence, it is a HVS commutation because it happens while the voltage across the switch T_2 is high.

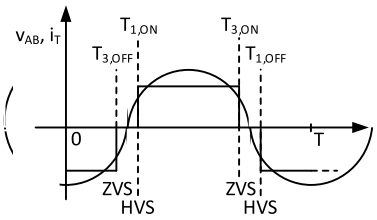

FIGURE 5. Commutation of the upper switches with PST.

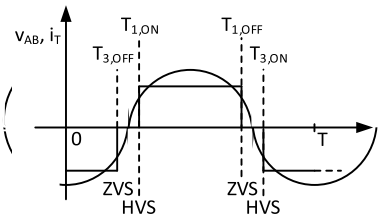

FIGURE 6. Commutation of the upper switches with anti-PT.

TABLE 1. Switching on voltages with PST.

	T_1	T_2	T_3	T_4
$i_T<0$	ZVS	HVS	HVS	ZVS
$i_T>0$	HVS	ZVS	ZVS	HVS

If the sign of the current were opposite to that shown in Fig. 5, the commutations would occur according to the cells highlighted in grey in Table 1. However, being the WPT systems designed to charge the battery, usually the sign of i_T complies with Fig. 5.

According to Table 1, the leg A of the HFI, formed by the switches T_1 and T_2, is subjected to higher solicitations than the right leg, formed by T_3 and T_4. This difference could lead to an uneven distribution of the faults of the HFI and necessitate oversizing one pair of switches with respect to the other.

B. HARMONIC CONTENT

The supply voltage v_{AB} expressed in terms of its Fourier series is

$$v_{AB}(t) = \frac{a_{0f_N}}{2} + \sum_{n=1}^{\infty}\left[a_{nf_N}\cos\left(\frac{2\pi}{T}nt\right) + b_{nf_N}\sin\left(\frac{2\pi}{T}nt\right)\right], \quad (1)$$

with the Fourier coefficients a_{nFN} and b_{nfN} defined as

$$a_{nf_N} \triangleq \frac{2}{T}\int_{-T/2}^{T/2} v_{AB}(t)\cos\left(\frac{2\pi}{T}nt\right)dt \quad (2)$$

$$b_{nf_N} \triangleq \frac{2}{T}\int_{-T/2}^{T/2} v_{AB}(t)\sin\left(\frac{2\pi}{T}nt\right)dt. \quad (3)$$

More conveniently, the Fourier series of v_{AB} can be written in the form

$$v_{AB}(t) = \frac{a_{0f_N}}{2} + \sum_{n=1}^{\infty} A_{nf_N}\sin\left(\frac{2\pi}{T}nt + \varphi_{nf_N}\right), \quad (4)$$

where the magnitude and the phase are derived from (1)-(3) according to

$$A_{nf_N} \triangleq \sqrt{{a_{nf_N}}^2 + {b_{nf_N}}^2} \quad (5)$$

$$\varphi_{nf_N} \triangleq atan\left(\frac{a_{nf_N}}{b_{nf_N}}\right). \quad (6)$$

Application of (2) and (3) to the waveform reported in Fig. 2 gives the Fourier coefficients

$$a_{nf_N} = \frac{2}{\pi}V_{dc}\frac{1}{n}\left[\cos(n\pi)\sin(n\pi\delta_{PST}) - \sin(n\pi\delta_{PST})\right] \quad (7)$$

$$b_{nf_N} = 0, \quad (8)$$

where the duty cycle δ_{PST}, given by

$$\delta_{PST} \triangleq \frac{\phi}{\pi} \quad (9)$$

has been defined to make it easier to compare with the results reported in the next Sections.

According to (5) and (6), the magnitude A_{nfN} of the n^{th} harmonic results equal to the absolute value of a_{nfN} whilst the initial phase of the n^{th} harmonic is $\pi/2$ or $-\pi/2$ according to the sign of a_{nfN}. The magnitude of the 1^{st} harmonic of v_{AB} is given by the well-known expression

$$A_{1f_N} = \frac{4}{\pi}V_{dc}\sin(\pi\delta_{PST}) = \frac{4}{\pi}V_{dc}\sin\left(\frac{\phi}{2}\right) \quad (10)$$

and its phase is $-\pi/2$.

From (7) and (8) it is easily derived that the odd harmonics have amplitudes that decrease with n whilst all the even harmonics, including also the direct component, have amplitudes equal to zero.

IV. ANTI-PHASE TECHNIQUE ANALYSIS

When the anti-PT is used, the commutations represented in Fig. 5 change into those sketched in Fig. 6, obtained from Fig. 3. Also in this case, the drawing has been simplified by considering a nearly sinusoidal waveform for the current i_T.

A. COMMUTATIONS

By the same considerations reported in Subsection III-A, it can be found that the HVS and ZVS commutations happen as it is shown in Fig. 6 and reported in the cells with the white background of Table 2. If the sign of i_T were opposite to that shown in Fig. 6, the commutations would occur according to the marks in the table cells with the gray background. With the help of Table 2, and remembering that the switching off of T_1 and T_3 entails a switching on of T_2 and T_4, it can be concluded that now for each leg of the HFI one commutation occurs with a low voltage applied across the switch, whilst the other occurs with a high voltage. Thus, the commutation solicitations are evenly shared among the HFI legs.

TABLE 2. Switching on voltages with anti-PT.

	T_1	T_2	T_3	T_4
$i_T<0$	ZVS	HVS	HVS	ZVS
$i_T>0$	HVS	ZVS	ZVS	HVS

B. HARMONIC CONTENT

The harmonic content of the supply voltage generated by the anti-P technique is analyzed by applying (2) and (3) to the waveform reported in Fig. 3. The obtained Fourier coefficients are

$$a_{nf_N} = \frac{2}{\pi} V_{dc} \frac{1}{n} \left[cos\left(n\pi\right) sin\left(n\pi\,\delta_A\right) - sin\left(n\pi\,\delta_B\right) \right] \quad (11)$$

$$b_{nf_N} = 0. \quad (12)$$

The initial phase of the n^{th} harmonic is $\pi/2$ or $-\pi/2$ according to the sign of a_{nfN}.

The zero-order coefficient α_{0fN}, i.e., twice the direct component of v_{AB}, is

$$a_{0f_N} = 2V_{dc}\left(\delta_A - \delta_B\right). \quad (13)$$

Comparison of (11) and (12) with (7) and (8) shows that if $\delta_A = \delta_B = \delta_{PST}$, the anti-PT generates the same harmonics, and hence the same v_{AB} waveform, as the PST.

However, the condition of having $\delta_A = \delta_B$ is not compulsory. Instead, the anti-PT allows the use any combination of δ_A and δ_B, provided that the relations

$$0 \le \delta_A \le 1, 0 \le \delta_B \le 1 \quad (14)$$

are fulfilled.

When $\delta_A \neq \delta_B$, according to (13), v_{AB} encompasses a direct component. Even when PST is applied, it is possible that v_{AB} encompasses a direct component due to the non-ideal operation of the HFI or of its control systems. Some considerations about its effects are given in the next Subsection.

By (5), (11), and (12), the magnitude A_{1fN} of the 1^{st} harmonic of v_{AB} results in

$$A_{1f_N} = \frac{2}{\pi} V_{dc} \left| sin\left(\pi\,\delta_A\right) + sin\left(\pi\,\delta_B\right) \right|. \quad (15)$$

It is mapped as a function of δ_A and δ_B in Fig. 7. The maximum of A_{1fN} is $4/\pi \cdot V_{dc,T}$, like in PST, and is reached at the point $A_1(1/2, 1/2)$, where $\delta_B = 1/2$ and $\delta_A = 1/2$. The corresponding value of a_{1fN} is $-4/\pi \cdot V_{dc,T}$ and the initial phase of the 1^{st} harmonic is $-\pi/2$. The figure shows that on its borders, where only one of the HFI legs is switched, the 1^{st} harmonic of v_{AB} is not equal to zero. In particular, the four points $B_1(1/2, 0)$, $B_2(0, 1/2)$, $B_3(1/2,1)$, and $B_4(1,1/2)$ exist where it reaches the amplitude $2/\pi V_{dc,T}$, i.e., half of the maximum amplitude reached at the point A_1.

The magnitude of the 3^{rd} harmonic is mapped in Fig. 8. It shows that some combinations (δ_A, δ_B) exist that nullify the magnitude of the 3^{rd} harmonic even if the corresponding magnitude of the 1^{st} harmonic is not null.

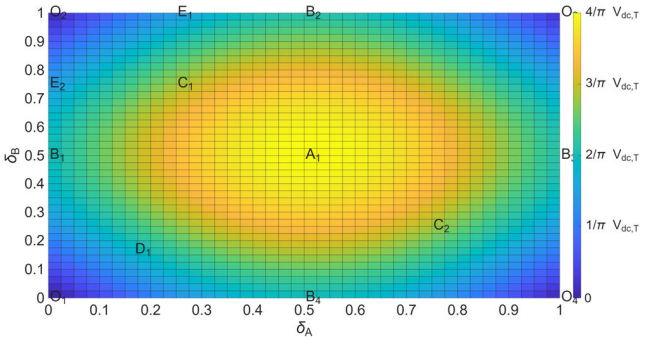

FIGURE 7. Magnitude A_{1fN} of the 1^{st}harmonic of v_{AB} obtained with the anti-PT as a function of δ_A and δ_B.

The condition by which the magnitude of an odd harmonic is zero is derived from (11) in the form

$$sin\left(n\pi\,\delta_A\right) = -sin\left(n\pi\,\delta_B\right), \quad (16)$$

whose solutions are

$$\delta_B = -\delta_A + \frac{2k}{n}, \delta_B = \delta_A + \frac{(2k+1)}{n}, k \in \mathbb{Z}. \quad (17)$$

From (17) it follows that it is possible to nullify the 1^{st} harmonic only if the pair (δ_A, δ_B) is equal to one of the pairs (0,0), (1,1), derived from the first of (17) with $k = 0$ and $k = 1$, or (0,1), (1,0), derived from the second of (17) with $k = 0$ and $k = -1$. This condition is confirmed by Fig. 7, which shows that A_{1fN} is equal to 0 only in the corners $O_1(0, 0)$, $O_2(0, 1)$, $O_3(1, 1)$, and $O_4(1, 0)$ of the square map where the pair (δ_A, δ_B) satisfies (14).

Differently from the 1^{st} harmonic, infinite pairs of δ_A and δ_B satisfying (17) can be found to nullify the odd harmonics of higher order. As an example, the 3^{rd} harmonic is nullified in the same pairs found for the first one, this time obtained with $k = 0$, $k = 3$, $k = 1$, and $k = -2$, or if one of the following conditions is matched:

$$\delta_B = -\delta_A + \frac{2}{3}, \quad \delta_B = -\delta_A + \frac{4}{3}$$
$$\delta_B = \delta_A + \frac{1}{3}, \quad \delta_B = \delta_A - \frac{1}{3}. \quad (18)$$

The first and the second conditions are solutions of the first of (17) with $k = 1$ and $k = 2$ whilst the third and the fourth are obtained solving the second of (17) with $k = 0$ and $k = -1$. The solutions listed above correspond to the corners of Fig. 8 and to the four straight lines mapped with the dark blue.

Being the dark blue lines the loci where the sign of a_{3fN} changes, they also correspond to the (δ_A, δ_B) pairs where the phase of the 3^{rd} harmonic changes from $-\pi/2$ to $\pi/2$ and vice versa.

Considering the even harmonics, (16) changes into

$$sin\left(n\pi\,\delta_A\right) = sin\left(n\pi\,\delta_B\right), \quad (19)$$

which gives

$$\delta_B = \delta_A + \frac{2k}{n}, \delta_B = -\delta_A + \frac{(2k+1)}{n}, k \in \mathbb{Z}. \quad (20)$$

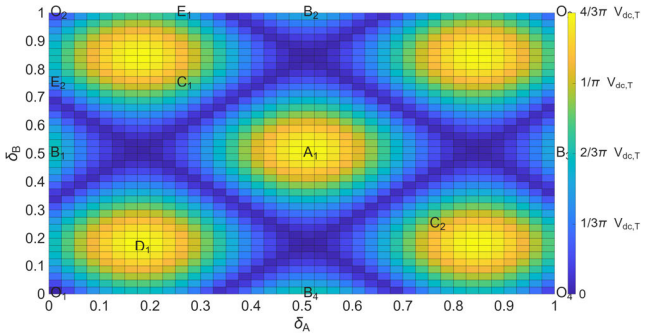

FIGURE 8. Magnitude A_{3fN} of the 3rd harmonic of v_{AB} obtained with the anti-PT as a function of δ_A and δ_B.

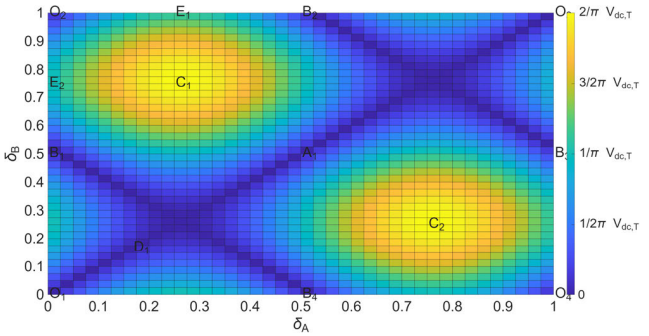

FIGURE 9. Magnitude A_{2fN} of the 2nd harmonic of v_{AB} obtained with the anti-PT and the in-PT as a function of δ_A and δ_B.

Besides the solutions at the corners of the square, from (20) the following solutions are obtained:

$$\delta_B = \delta_A, \delta_B = -\delta_A + \frac{1}{2}, \delta_B = -\delta_A + \frac{1}{2}. \tag{21}$$

The first of them comes from the first of (20) with k = 0, whilst the second and the third come from the second of (20) with k = 0 and k = −1. They correspond to the dark blue straight lines of Fig. 9, which maps the magnitude of the 2nd harmonic of v_{AB}.

The figure shows that two points C_1(1/4, 3/4) and C_2(3/4, 1/4) exist where the 2nd harmonic of v_{AB} reaches the maximum value $2/\pi \cdot V_{dc,T}$, i.e., one half of the maximum value reached by the 1st harmonic of v_{AB}. On the borders of the map the amplitude of the 2nd harmonic of v_{AB} is different from zero and reaches its maximum value $1/\pi \cdot V_{dc,T}$ in the eight points located at distance 1/4 from the corners of the map

In general, the critical pairs (δ_A, δ_B) where the maximum amplitude of the nth harmonic could occur are found by solving the equations

$$\begin{aligned} \frac{\partial a_{nf_N}}{\partial \delta_A} = 0 &\underset{\square}{\Rightarrow} cos\,(n\pi\,\delta_A) = 0 \Rightarrow \delta_A = \frac{1}{2n} + \frac{k_A}{n}, k_A \in \mathbb{Z} \\ \frac{\partial a_{nf_N}}{\partial \delta_B} = 0 &\underset{\square}{\Rightarrow} cos\,(n\pi\,\delta_B) = 0 \Rightarrow \delta_B = \frac{1}{2n} + \frac{k_B}{n}, k_B \in \mathbb{Z}. \end{aligned} \tag{22}$$

In setting the values of k_A and k_B, the conditions (14) must be fulfilled. As an example, Tab. 3 lists some combinations of n, k_A and k_B that fulfill both (22) and (14) and the corresponding values of δ_A and δ_B.

In order to distinguish between the maxima and the saddle points of A_{nfN}, the sign of the second order partial derivative of (11) with respect to δ_A and of the discriminant of the Hessian of (11) must be computed in the critical pairs (δ_A, δ_B) found by (22).

The second order derivative in the critical pairs results

$$\frac{\partial^2 a_{nf_N}}{\partial {\delta_A}^2} = -2V_{dc,T} n\pi\, cos\,(n\pi)\, sin\left(\frac{\pi}{2} + k_A\pi\right). \tag{23}$$

TABLE 3. Conditions for maxima, minima, and saddle points of a_{nfN}.

n	k_A	k_B	δ_A	δ_B	anti-P	in-P
1	0	0	1/2	1/2	min	saddle
2	0	0	1/4	1/4	saddle	saddle
2	0	1	1/4	3/4	max	max
2	1	0	3/4	1/4	min	min
2	1	1	3/4	3/4	saddle	saddle
3	0	0	1/6	1/6	min	saddle
3	0	1	1/6	1/2	saddle	max
3	0	2	1/6	5/6	min	saddle
3	1	0	1/2	1/6	saddle	min
3	1	1	1/2	1/2	max	saddle
3	1	2	1/2	5/6	saddle	min
3	2	0	5/6	1/6	min	saddle
3	2	1	5/6	1/2	saddle	max
3	2	2	5/6	5/6	min	saddle

whilst the discriminant of the Hessian matrix is

$$\Delta = -4V_{dc,T}^2 n^2\pi^2 cos\,(n\pi)\, sin\left(\frac{\pi}{2} + k_A\pi\right) sin\left(\frac{\pi}{2} + k_B\pi\right) \tag{24}$$

If $\Delta > 0$ and $\partial^2 a_{nfN}/\partial {\delta_A}^2 < 0$, the critical pair lays on a maximum of a_{nfN}, whereas if $\Delta > 0$ and $\partial^2 a_{nfN}/\partial {\delta_A}^2 > 0$, the critical pair lays on a minimum of a_{nfN}. In both these cases the critical pair (δ_A, δ_B) corresponds to a maximum of A_{nfN}. On the contrary, if $\Delta < 0$ the critical pair lies on a saddle point of a_{nfN}.

Considering the expressions (23) and (24), and different combinations of n, k_A, and k_B, Tab. 4 concerning the nature of the critical pairs is obtained. With its help, the penultimate column of Tab. 3 has been filled. It should be noted that the saddle points of a_{nfN} lie on the intersections of the lines where $A_{nfN} = 0$, clearly visible in Figs. 8 and 9.

From the previous analysis, it can be concluded that the anti-PT can be used to reproduce the same behavior as the PST, but with a more evenly distributed solicitation of the power switches that constitute the HFI. Moreover, since anti-PT has two degrees of freedom instead of only one,

TABLE 4. Critical pairs for the anti-P and the in-P techniques.

n	k_A	k_B	max	min	saddle
even	even	even			X
even	even	odd	X		
even	odd	even		X	
even	odd	odd			X
odd	even	even		X	
odd	even	odd			X
odd	odd	even			X
odd	odd	odd	X		

it exhibits some additional features that could be profitably exploited.

C. VOLTAGE DIRECT COMPONENT

Depending on the actual topology of the compensation network connected to the transmitting coil, the direct component of v_{AB} could cause the flow of a direct current in the transmitting coil. This current component will not give rise to any power transfer but, instead, it will increase the Joule losses in the transmitting coil and in the power switches of the HFI. Moreover, it could lead to the saturation of the ferrite core of the transmitting coil, thus causing a decrease in the coupling coefficient of the coil pair.

In the series compensation, used in the scheme of Fig. 1, the capacitor that constitutes the compensation network inherently avoids the circulation of any direct current component. Similarly, the CLC compensation [19], shown in Fig. 10a, requires a capacitor C_1 to be connected in series with the HFI output, therefore it also intrinsically blocks the flow of the direct current component. In the LLC compensation topology [20], [21], shown in Fig. 10b, there is no capacitor connected directly to the HFI output, however the overall action of C_1 and C_2 prevents direct current from flowing through the transmitting coil L_T and the filter coil L_1. The same topology can be found also when the switched capacitance technology is exploited [22]. If other compensation topologies are selected, such as the LCL topology, the capacitor is inserted at the HFI output as an additional component [23] specifically to block the direct component of i_T, as shown in Fig. 10c. In CLC and LCC topologies it is possible that by design, or because of load or coupling coefficient variations, the reactance of L_T plus the reactance reflected from the receiving section of the WPTS resonates with the reactance of C_2 at the frequency of one of the harmonics of v_{AB}. This condition, however, would not impair the blocking effect of C_2 on the direct component of i_T because the resonance cannot happen at frequency equal to zero.

Following from these considerations, in the subsequent analysis the effects of the direct components of v_{AB} will be disregarded.

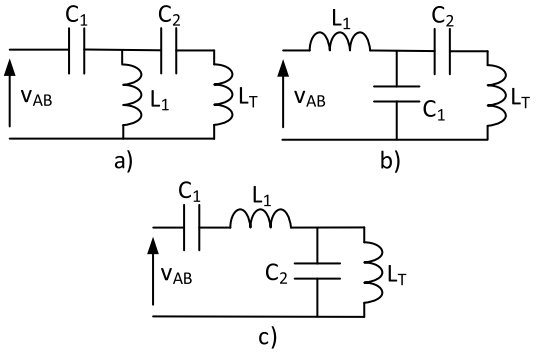

FIGURE 10. a) CLC topology, b) LCC topology, c) LCL topology with blocking capacitor.

TABLE 5. Switching on voltages with in-PT (Fig. 11a).

	T_1	T_2	T_3	T_4
$i_T<0$	ZVS	HVS	HVS	ZVS
$i_T>0$	HVS	ZVS	ZVS	HVS

V. IN-PHASE TECHNIQUE ANALYSIS

Use of the in-PT entails that the commutations of the upper switches happen according to Fig. 11a or Fig. 11b. In both the figures, a nearly sinusoidal waveform has been considered for i_T.

A. COMMUTATIONS

Fig. 11a is relevant to the condition by which the current i_T changes its sign while v_{AB} is positive. The marks ZVS and HVS highlight that during the supply period each leg of the HFI turns on one switch while the applied voltage is high and the other switch while the applied voltage is low. Thus, it can be concluded that the in-PT evenly shares the solicitation between the HFI legs, as it is shown by the cells of Table 5 with a white background. With different values of δ_A and δ_B the pulses of v_{AB} could lie completely in the interval where i_T is positive, as shown in Fig. 11b, in this case, the commutations happen according to the cell of Table 6 with a white background.

If the sign of i_T were opposite to that shown in Fig. 11, the cells with the gray background of Tables 5 and 6 must be considered. In any case, the ZVS and HVS commutations are evenly shared between the two legs of the HFI.

The next Subsection will show that the in-PT allows nullifying the 1st harmonic of v_{AB} while at the same time generating a 2nd harmonic. Hence, it is worth analyzing the commutations under the hypothesis that i_S has a frequency corresponding to that of the 2nd harmonic of v_{AB}, i.e. twice the switching frequency. This condition is represented in Fig. 12. Also in this case, the HVS and ZVS commutations are evenly shared. As an example, in the situation sketched in Fig. 12, commutations happen according to the second row of Table 5.

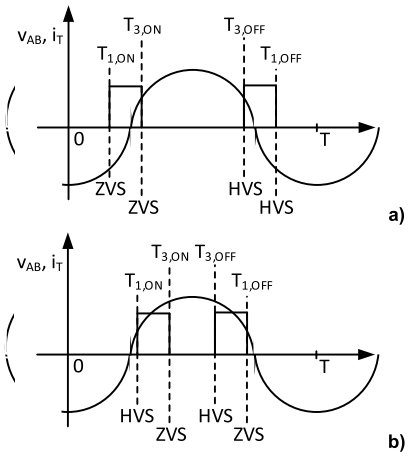

FIGURE 11. Commutation of the upper switches with in-PT considering i_T changing its sign while $v_{AB} > 0$ a) or while $v_{AB} = 0$ b).

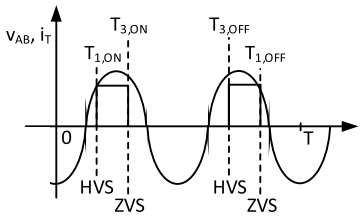

FIGURE 12. Commutation of the upper switches with in-PT considering i_T having twice the frequency of v_{AB}.

TABLE 6. Switching on voltages with in-PT (Fig. 11b).

	T_1	T_2	T_3	T_4
$i_T<0$	ZVS	HVS	HVS	ZVS
$i_T>0$	HVS	ZVS	ZVS	HVS

B. HARMONIC CONTENT

The Fourier coefficients of v_{AB} for the in-PT are

$$a_{nf_N} = \frac{2}{\pi} V_{dc,T} \frac{1}{n} cos\,(n\pi)\,[sin\,(n\pi\,\delta_A) - sin\,(n\pi\,\delta_B)] \quad (25)$$

$$b_{nf_N} = \frac{2}{\pi} V_{dc,T} \frac{1}{n} sin\,(n\pi)\,[sin\,(n\pi\,\delta_A) - sin\,(n\pi\,\delta_B)]\,. \quad (26)$$

Fig. 11 shows that v_{AB} has a direct component, indeed, the coefficient a_{0fN} maintains the same expression as in (13). The considerations reported in Section III.C regarding the direct component of v_{AB} hold also for the in-PT.

Following from (5) and (6), the magnitude and the phase of the n^{th} harmonic are

$$A_{nf_N} = \frac{2}{\pi} V_{dc,T} \frac{1}{n} |sin\,(n\pi\,\delta_A) - sin\,(n\pi\,\delta_B)|\,, \quad (27)$$

$$\varphi_{nf_N} = atan\left[\frac{cos\,(n\pi)}{sin\,(n\pi)}\right] = \frac{\pi}{2} - n\pi. \quad (28)$$

The magnitude of the even harmonics is equal to that one obtained with the anti-PT, and hence the map of the amplitude A_{2fN} is the same as in Fig. 9. For the odd harmonics, the

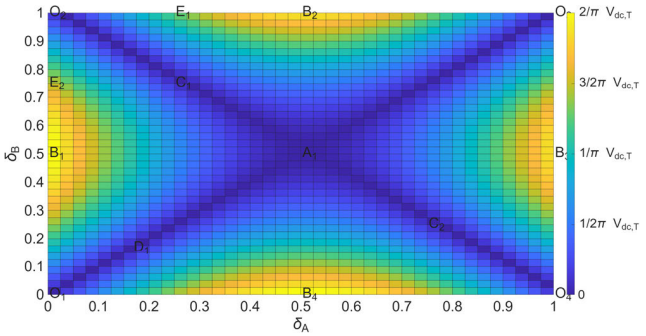

FIGURE 13. Magnitude A_{1fN} of the 1st harmonic of v_{AB} obtained with the in-PT as a function of δ_A and δ_B.

sign of the first addendum on the right-hand side of (27) is positive instead of negative. This difference entails that any harmonic, whether even or odd, can be nullified by imposing the condition (20).

In particular, the 1st harmonic has zero magnitude if one of the two following conditions, obtained from (20) setting k = 0, holds

$$\delta_B = \delta_A,\ \delta_B = -\delta_A + 1. \quad (29)$$

This result is confirmed by Fig. 13, which shows the map of A_{1fN}. The maximum of A_{1fN} is reached when $\sin(\pi\,\delta_A) = 1$ and $\sin(\pi\,\delta_B) = 0$ or when $\sin(\pi\,\delta_A) = 0$ and $\sin(\pi\,\delta_B) = -1$. Its value is $2/\pi\,V_{dc,T}$, i.e., one half of the maximum 1st harmonic magnitude reached with the anti-PT.

For the 3rd harmonic, from (20) the following relations are obtained for δ_A and δ_B.

$$\delta_B = \delta_A,\quad \delta_B = -\delta_A + \frac{1}{3},\quad \delta_B = \delta_A + \frac{2}{3}$$
$$\delta_B = -\delta_A + 1,\quad \delta_B = -\delta_A + \frac{5}{3},\quad \delta_B = \delta_A - \frac{2}{3}. \quad (30)$$

They are confirmed by the map plotted in Fig. 14.

Analysis of the second of (20) shows that for any odd n exists a k such that $\delta_B = -\delta_A + 1$ is a solution of (19). Hence, imposing this relation between δ_A and δ_B, it is possible to obtain a supply voltage v_{AB} that is formed only by the even harmonics and that, according to Fig. 9, reaches the maximum of A_{2fN} at points C_1 and C_2.

Following from (27), the maxima of A_{nfN} occur in correspondence with the maxima and the minima of

$$\tilde{A}_{nf_N} = \frac{2}{\pi} V_{dc,T} \frac{1}{n} [sin\,(n\pi\,\delta_A) - sin\,(n\pi\,\delta_B)]\,. \quad (31)$$

Like for the anti-PT, the critical pairs where the partial derivatives of $\tilde{A}_{nfN}$ are equal to zero are given by (22). The second order derivative computed in the critical pairs results

$$\frac{\partial^2 \tilde{A}_{nf_N}}{\partial {\delta_A}^2} = -2V_{dc,T} n\pi\, sin\left(\frac{\pi}{2} + k_A\pi\right), \quad (32)$$

whereas the discriminant of the Hessian matrix is given by

$$\Delta = -4V_{dc,T}^2 n^2\pi^2 sin\left(\frac{\pi}{2} + k_A\pi\right) sin\left(\frac{\pi}{2} + k_B\pi\right). \quad (33)$$

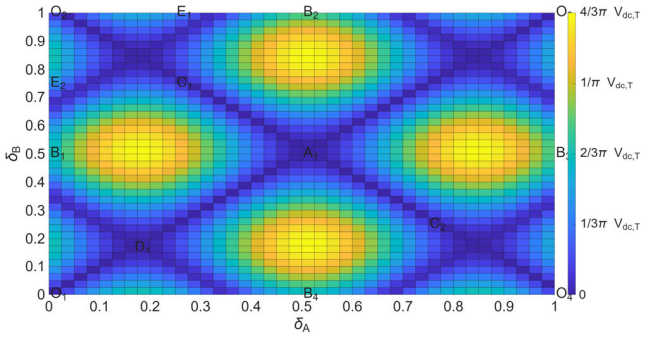

FIGURE 14. Magnitude A_{3fN} of the 3rd harmonic of v_{AB} obtained with the in-PT as a function of δ_A and δ_B.

TABLE 7. Conditions for maxima, minima, and saddle points of $\tilde{A}_{NF_N}$.

k_A	k_B	max	min	saddle
even	even			X
even	odd	X		
odd	even		X	
odd	odd			X

Differently from (23) and (24), neither of them is a function of n and, consequently, the nature of the critical points depends only on k_A and k_B, according to Tab. 7. The rules listed in Tab. 7 have been applied to the critical pairs of $\tilde{A}_{nf_N}$ for n = 1, 2, and 3 to determine their behavior, listed in the rightmost column of Tab. 1.

VI. CONTROL STRATEGIES

The performances of the proposed modulation techniques have been tested and compared with those of the PST from the point of view of the voltage and current waveforms and of the HFI efficiency. In order to exploit the two degrees of freedom offered by the anti-PT and the in-PT, simple control strategies that involve only horizontal, vertical or diagonal paths on the (δ_A, δ_B) maps are considered, leaving the optimization of the paths to a subsequent work.

The strategies are divided into two groups, depending whether the HFI switching frequency is set to f_N, with the 1st harmonic of v_{AB} giving the useful voltage component, or to $f_N/2$, with the useful component of v_{AB} being its 2nd harmonic. All the strategies follow paths that start with zero output voltage and end with the maximum amplitude of useful output voltage. Only two of the considered strategies allow reaching the maximum harmonic amplitude $A_{1fN} = 4/\pi \cdot V_{dc,T}$ at the point A_1 and both of them exploit the 1st harmonic of v_{AB}. Adopting the other strategies, the maximum amplitude of the useful harmonic reaches $2/\pi \cdot V_{dc,T}$ or $1/\pi \cdot V_{dc,T}$, nevertheless, these strategies are worth considering because they enable achieving higher efficiency operations of the WPTS.

Thanks to the symmetry of the maps reported in Figs. 7, 8, 9, 13, and 14, any of the strategies described below can be implemented using different paths with symmetrical starting and ending points. In the following discussion, only some of the paths are considered because the derivation of the others is straightforward.

A. STRATEGIES WITH SWITCHING FREQUENCY EQUAL TO F_N

When the switching frequency is equal to the resonant frequency f_N of the coil-capacitor series, the useful component of the supply voltage generated by the HFI corresponds to its 1st harmonic. Consequently, in order to reach the maximum amplitude $4/\pi \cdot V_{dc,T}$ of the supply voltage, it is necessary to use the anti-PT. Instead, if a supply voltage with an amplitude less than or equal to is required $2/\pi \cdot V_{dc,T}$, it is also possible to use the in-PT, according to the map in Fig. 13.

1) STRATEGY 1 (ANTI-PT)

As shown in the previous Sections, the maximum 1st harmonic amplitude of $4/\pi \cdot V_{dc,T}$ can be reached only by the anti-PT operating at point A_1. According to the map of Fig. 7, the required voltage interval from 0 to $4/\pi \cdot V_{dc,T}$ can be covered by setting the initial value of the (δ_A, δ_B) pair to the point O_1(0, 0), and then moving along the diagonal path $\delta_B = \delta_A$ till reaching the center of the map in A_1(1/2, 1/2). This is the same path followed when the conventional PST is implemented. According to Figs. 8 and 9, along this path the amplitude of the 2nd harmonic of v_{AB} is always equal to zero whereas the 3rd harmonic reaches its maximum value of $4/3\pi \cdot V_{dc,T}$ in the two points D_1(1/6, 1/6) and A_1.

2) STRATEGY 2 (ANTI-PT)

The anti-PT allows reaching the central point A_1 following a different path that starts at the point O_2(0, 1) of the map in Fig. 7 and is defined by the relation $\delta_B = 1\text{-}\delta_A$. Strategy 2 follows this path and reaches A_1 passing through the point C_1(1/4,3/4) of Fig. 9, where the 2nd harmonic reaches its maximum amplitude.

3) STRATEGY 3 (ANTI-PT)

In order to increase the efficiency of the system, the anti-PT can be used following paths that require the switching of only one leg of the HFI. These paths correspond to the borders of the maps. For example, from the starting point O_1 of Fig. 7, the vertical path that reaches the point B_1(0, 1/2) can be followed maintaining $\delta_A = 0$ and increasing δ_B from 0 to 0.5. At the point B_1 the 1st harmonic of v_{AB} has amplitude $2/\pi \cdot V_{dc,T}$. In order to further increase the voltage, it is necessary to enable the switching of the other HFI leg to follow the horizontal path from B_1 to A_1.

4) STRATEGY 4 (IN-PT AND ANTI-PT)

Fig. 13 shows that the in-PT generates a 1st harmonic component that reaches its maximum value of $2/\pi \cdot V_{dc,T}$ at point B_1. Thus, a possible strategy consists of moving from O_1 to B_1 commanding the HFI according to the in-PT, and then increasing the generated voltage up to $4/\pi \cdot V_{dc,T}$ by enabling

the anti-PT and moving along the paths B_1-A_1, as described dealing with Strategy 3.

B. STRATEGIES WITH SWITCHING FREQUENCY EQUAL TO $F_N/2$

Reducing the switching frequency of the HFI is another viable and effective approach to decreasing its switching losses and to increasing its efficiency. Indeed, the in-PT has been conceived specifically to operate at half of the nominal supply frequency. On the other side, Fig. 9 shows that even anti-PT generates a voltage component at the second harmonic which can be used to supply the transmitting coil if the switching frequency is set at $f_N/2$.

1) STRATEGY 5 (IN-PT)

In order to take advantage of the lower switching losses assured by the in-PT, Strategy 5 follows a path that starts from the point O_2 of Fig. 8, where $A_{2fN} = 0$ and then moves according to relation $\delta_B = 1\text{-}\delta_A$ to the point C_1, where $A_{2fN} = 2/\pi \cdot V_{dc,T}$. This is the same path followed in Strategy 2, but now the in-PT is enabled and the HFI operates at $f_N/2$ so that the useful component of v_{AB} is its 2nd harmonic instead of the first one.

2) STRATEGY 6 (ANTI-PT)

The map of Fig. 9 applies for anti-PT as well. Hence, Strategy 5 can be applied operating the HFI with the anti-PT, setting the switching frequency to $f_N/2$ along the path O_2-C_1. This approach provides the advantage of implementing only one commutation technique, operated at the switching frequency f_N or $f_N/2$, according to the required output voltage. The disadvantage is the generation of a voltage that encompasses an unwanted 1st harmonic component along the path O_2-C_1, thus increasing the resonant capacitor solicitations.

3) STRATEGY 7 (IN-PT)

As was done in Strategy 3, the HFI losses are reduced by switching only one of its legs. According to Fig. 9, this can be done by enabling the in-PT and moving from point O_2 to $E_1(1/4, 1)$ maintaining $\delta_B = 1$. The maximum 2nd harmonic amplitude reached in E_1 is $1/\pi \cdot V_{dc,T}$, i.e., one half of the voltage reached at point C_1. Then, in order to reach the maximum voltage available with the in-PT, it is possible to move from E_1 to C_1 along the vertical path $\delta_A = 1/4$.

4) STRATEGY 8 (ANTI-PT)

Strategy 8 follows the same path as Strategy 7, but it is implemented using the anti-PT instead of the in-PT.

VII. EXPERIMENTAL RESULTS

Experimental tests have been carried out on the experimental setup described in [18] and whose parameters are given in Tab.8. The prototype is equipped with an HFI made of SiC MOSFETs and has series-series compensation at both the transmitting and the receiving section. At the receiving section, the series of the coil and of the resonating capacitor is connected to the input of a diode rectifier. The dc bus voltage at the output of the rectifier is manipulated by a buck chopper that supplies the load.

TABLE 8. Parameters of the prototypal WPT system.

Transmitting coil self-inductance	L_T	120 µH
Receiving coil self-inductance	L_R	120 µH
Transmitting section resonant capacitor	C_T	30 nF
Receiving section resonant capacitor	C_R	30 nF
Transmitting coil parasitic resistance	R_T	0.5 Ω
Receiving coil parasitic resistance	R_R	0.5 Ω
Coil mutual inductance	M	30 µH
Nominal frequency	f_N	85 kHz
Equivalent load	R_{Leq}	5.6 Ω

The implementation of the two proposed modulation techniques and their use with the different control strategies only required a partial rewrite of the interrupt service routine executed by the microcontroller that generates the command signals for the HFI. Instead, no modifications to the hardware of the prototypal WPTS were necessary.

The waveforms relevant to the coil currents i_T and i_R, and to the HFI voltages v_{AO} and v_{BO} have been acquired using a Tektronix TDS5034 oscilloscope equipped with voltage and current probes. The v_{AO} and v_{BO} samples have been processed in the Matlab environment to compute the corresponding values of v_{AB}. The efficiency measurements have been performed by a Yokogawa WT1800 wattmeter.

The waveform samples and the efficiency measurements are plotted in the figures shown in the following Subsections.

A. WAVEFORM ANALYSIS

The first tests were focused on checking the actual waveforms of the voltages and currents obtained by implementing the two modulation strategies.

Fig. 15 reports the waveform of the two phase voltages v_{AO} and v_{BO}, of the supply voltage v_{AB} and of the current i_T obtained with the conventional PST and $\delta_{PST} \approx 0.4$. The dc bus voltage $V_{dc,T}$ has been set to only about 8V in order to highlight commutation phenomenon. Fig 16 reports the waveform of the same quantities obtained using the anti-PT with $\delta_A = \delta_B \approx 0.4$ and the same dc bus voltage. As expected, the waveforms of v_{AB} obtained with the two commutation techniques are quite similar and, consequently, the current waveforms are similar as well.

Instead, because of the different commutation techniques, the waveforms of the phase voltages v_{AO} and v_{BO} are completely different. Focusing the attention on the commutations, it can be easily recognized that in Fig. 15 both the commutation of v_{AO} exhibits sharp edges and a rectangular-shaped overvoltage in correspondence to the dead times. On the other hand, both the edges of v_{BO} are quite smoother. The

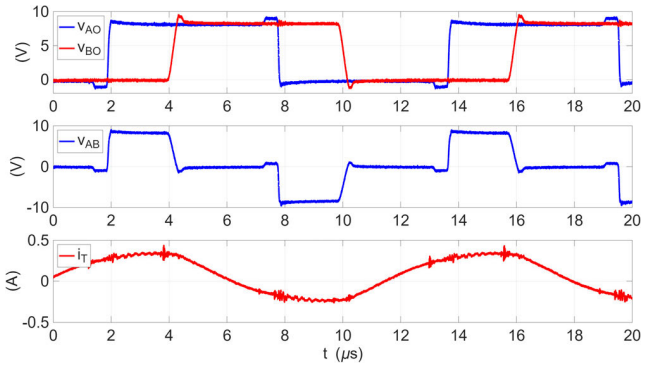

FIGURE 15. HFI phase voltages and output voltage and current waveforms obtained with the PST.

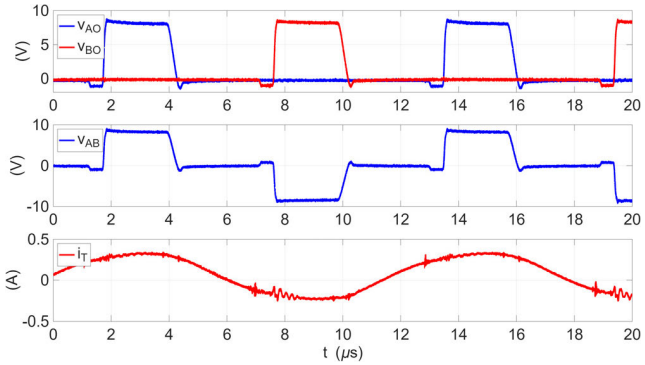

FIGURE 16. HFI phase voltages and output voltage and current waveforms obtained with the anti-PT.

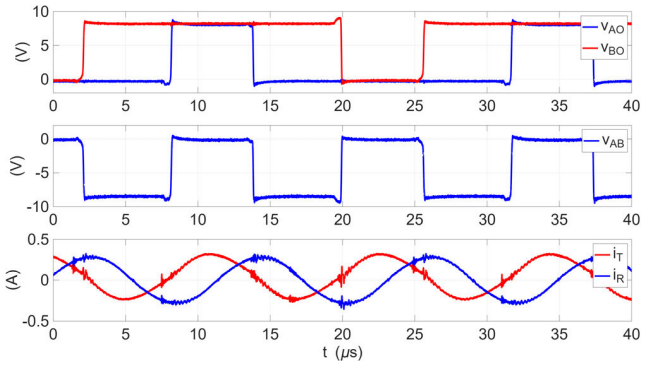

FIGURE 17. HFI phase and output voltages and coil currents waveforms obtained with the in-PT operating at $f_N/2$.

waveforms of Fig. 16 show that with the anti-PT both v_{AO} and v_{BO} have one sharp edge and one smooth edge with a more even share of the solicitation between the HFI legs.

The behavior of the WPTS when the in-PT is enabled is represented by Fig. 17. It is worth noting that the time scale of Fig. 17 is twice that of Figs. 15 and 16 because the switching frequency is now set to 42.5 kHz instead of 85 kHz. Nevertheless, according to the in-PT operation, the voltage v_{AB} oscillates at 85 kHz and, having set $\delta_A \approx 3/4$ and $\delta_B \approx 1/4$, it has a duty cycle of about 50%. Being the working point of the HFI about in C_2, according to Figs. 8 and 13,

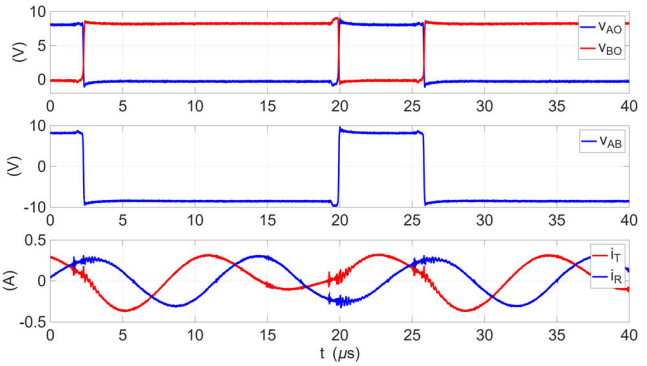

FIGURE 18. HFI phase and output voltages and coil currents waveforms obtained with the anti-PT operating at $f_N/2$.

the 2nd harmonic component of v_{AB}, i.e. its component at 85 kHz, has an amplitude of about $2/\pi \cdot V_{dc,T}$, whereas its 1st harmonic component, i.e. the component at 42.5 kHz, is about zero. Consequently, the current i_T in the transmitting coil is nearly perfectly sinusoidal, and the same condition holds for the current i_R in the receiving coil.

Maintaining the same switching frequency of 42.5 kHz and the same values for δ_A and δ_B but enabling the anti-PT instead of the in-PT, the voltage and current waveforms change into those reported in Fig. 18. The HFI is working at point C_2, like in the previous test, but, according to Figs. 7 and 9 and by (15), now the 1st harmonic component of v_{AB} has an amplitude of $2\sqrt{2}/\pi \cdot V_{dc,T}$ while the amplitude of the 2nd harmonic is still $2/\pi \cdot V_{dc,T}$. In these conditions, the current i_T is no longer sinusoidal. However, its 1st harmonic component is effectively attenuated by the compensation network. The combined action of the compensation network connected to the receiving coil makes the current i_R sinusoidal despite the harmonic content of i_T.

B. EFFICIENCY ANALYSIS

The efficiency analysis has been performed by programming in the firmware of the HFI the selected modulation technique and the relation between δ_B and δ_A, thus imposing the path to be followed, and then manually increasing δ_A step by step leaving to the firmware the computation of the corresponding δ_B. For each pair (δ_A, δ_B) the efficiency η_{inv} of the HFI, the total efficiency η_{tot} of the whole WPTS, and the power P_L transmitted to the load have been acquired by the wattmeter.

The relation η_{inv}-P_L relevant to the strategies 1 and 2 is reported in the top half of Fig. 19. As a comparison, the efficiency obtained implementing the PST is also reported in the figure. In all the three cases, P_L reached the maximum value of 130 W, which is defined as P_M, i.e., the maximum power of the system.

The bottom half of Fig. 19 plots the differences between η_{inv} achieved with the strategies 1 and 2 and the PST. The figure shows that Strategy 1, i.e. the anti-PT operating at f_N along the path O_1-A_1, has nearly the same efficiency performance as the PST, being its efficiency not more than

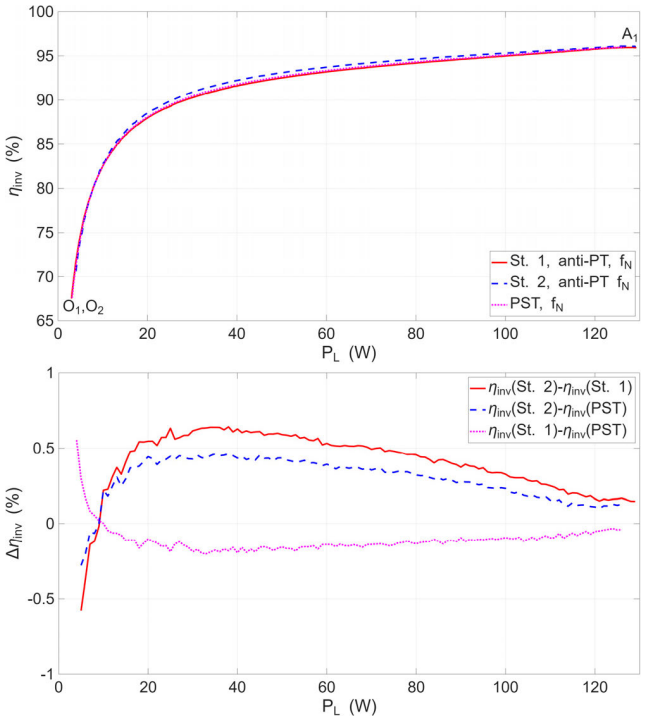

FIGURE 19. Efficiency of the HFI vs. transferred power with Strategy 1 and Strategy 2 (top). HFI efficiency difference between Strategy 1, Strategy 2, and PST (bottom).

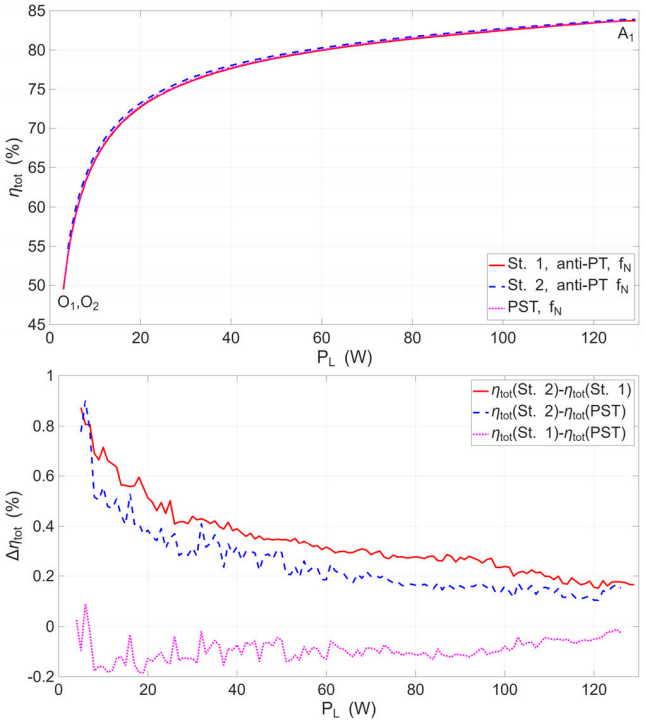

FIGURE 20. Efficiency of the WPTS vs. transferred power with Strategy 1 and Strategy 2 (top). WPTS efficiency difference between Strategy 1, Strategy 2, and PST (bottom).

0.2% lower than PST. This is not unexpected because the two commutation techniques generate the same voltage waveforms along the path. On the other hand, Strategy 2, which

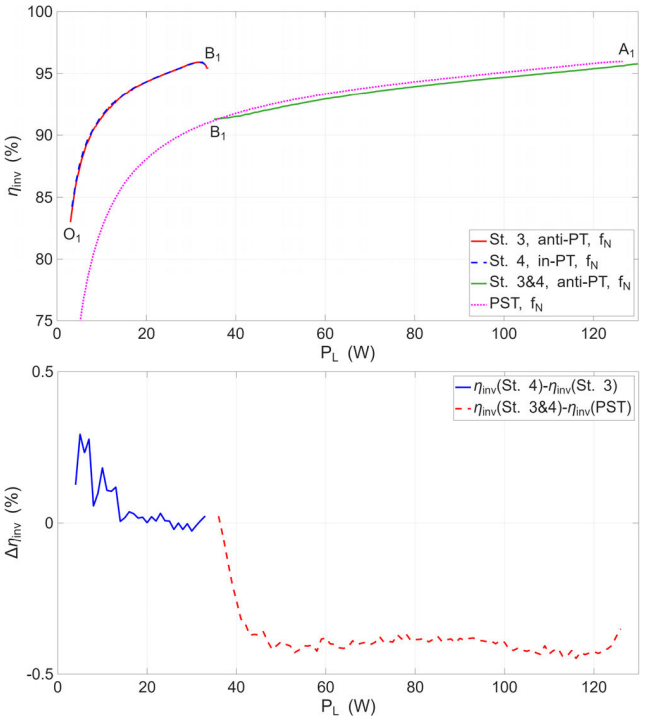

FIGURE 21. Efficiency of the HFI vs. transferred power with Strategy 3 and Strategy 4 (top). HFI efficiency difference between Strategy 4 and Strategy 3 and between Strategy 3& 4 and PST(bottom).

reaches the point A_1 moving from O_2 and passing through C_1, obtains an HFI efficiency more than 0.5% higher than the PST even if the generated voltage encompasses a 2nd harmonic component in the low-power region. These results are confirmed considering the overall efficiency η_{tot}, plotted in Figs. 20 top and bottom. Due to the losses of the coil coupling and of the rectifier, η_{tot} is obviously lower than η_{inv}, but in any case, Strategy 1 exhibits the nearly the same performance as the PST whilst Strategy 2 performs slightly better, especially in the low power region.

Strategies 3 and 4 exploit the vertical path O_1-B_1 on the left edge of the maps to reach the output voltage $2/\pi \cdot V_{dc,T}$, with a corresponding power equal to $P_M/4$. Despite this power limitation, the two strategies are worth considering because along this path only one leg of the HFI is switched and, consequently, its switching losses are halved. The top half of Fig. 21 confirms this condition and shows that along the path O_1-B_1 the obtained efficiency is more than 5% higher than that one of the PST, reported in the figure as a comparison. As shown on the left side of the bottom half of Fig. 21, the efficiency difference between Strategy 4 and Strategy 3 along the path O_1-B_1 is less than 0.25% even if Strategy 3 uses the anti-PT and Strategy 4 the in-PT. To further increase the output power, both Strategy 3 and Strategy 4 use the anti-PT along the path B_1-A_1 and hence they control the HFI in the same way. The left side of the bottom half of Fig. 21 shows that in this condition the efficiency of PST is up to 0.4% higher than that achieved by Strategy 3 and Strategy 4. The

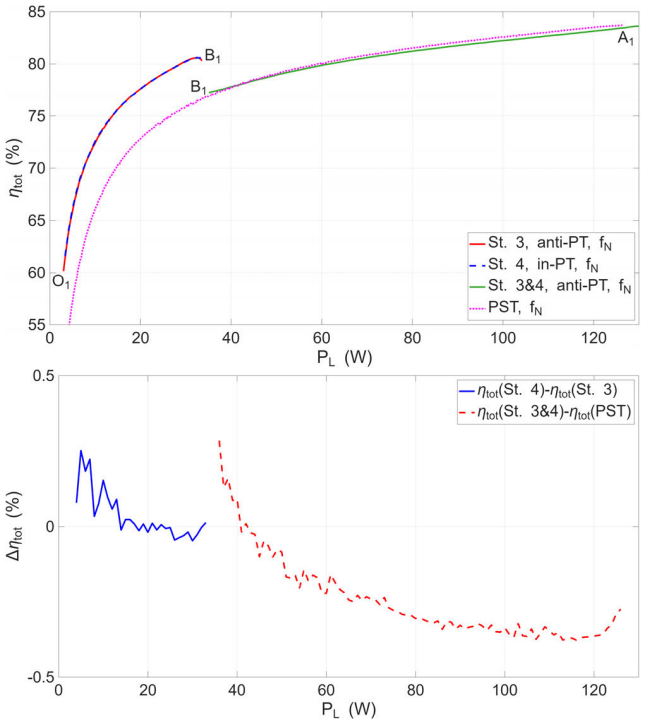

FIGURE 22. Efficiency of the WPTS vs. transferred power with Strategy 3 and Strategy 4 (top). WPTS efficiency difference between Strategy 4 and Strategy 3 and between Strategy 3&4 and PST(bottom).

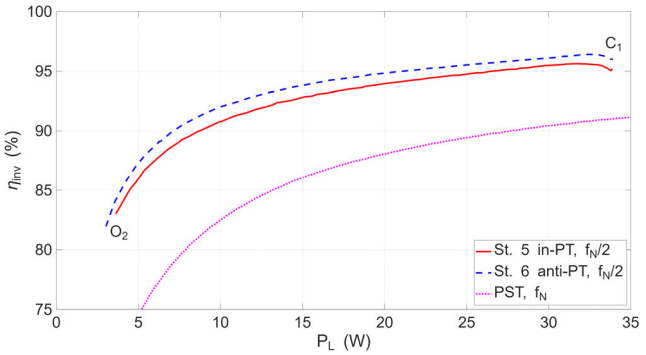

FIGURE 23. Efficiency of the HFI vs. transferred power with Strategy 5 and Strategy 6.

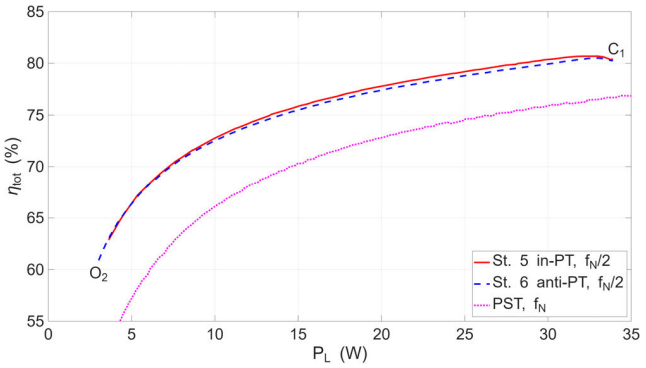

FIGURE 24. Efficiency of the WPTS vs. transferred power with Strategy 5 and Strategy 6.

corresponding efficiency of the whole WPTS is shown in Fig. 22. The comments relevant to η_{inv} hold also with regard to η_{tot}, with the difference that the efficiency gain with respect to the PST is reduced to about 3% because of the losses in the coil coupling and in the rectifier.

Strategies 5 and 6 reduce the HFI switching losses by halving the switching frequency instead of using only one leg of the HFI. As shown in Section IV-B, the maximum 1st harmonic amplitude of v_{AB} is equal to $2/\pi \cdot V_{dc,T}$. Consequently, also in this case the power transmitted to the load is limited to 1/4 P_M. However, as shown in Fig. 23, in this low power region the obtained efficiency is up to 15% higher than that of PST, with the anti-PT performing slightly better than the in-PT. Fig. 24 confirms that Strategies 5 and 6 outperform PST also from the perspective of the total efficiency, with an efficiency gain up to 10%.

When the required load power is very low, it is possible to enable Strategy 7 or Strategy 8. Beside operating at $f_N/2$, both of them initially follow the path O_2-E_1 along the border of the maps and hence only one leg of the HFI is switched so that the losses are further reduced. Fig. 25 shows that in this first part of the path, Strategy 7 outperforms Strategy 8 and maintains a nearly constant efficiency. In the second part of the path, from E_1 to C_1, Strategy 8 performs better than Strategy 7 but the difference is very small. In this low power interval, both strategies attain an HFI efficiency more than 22% higher than the PST. The advantage with respect to PST is maintained also when the total efficiency is considered, but in this case, it is reduced to about 15%. Moreover, along the path O_2-E_1, η_{tot} is nearly the same for both Strategy 7 and Strategy 8. In the load power range between 1/16 P_M and 1/4 P_M, both strategies perform slightly worse than Strategy 5 and Strategy 6 but, in any case, much better than the PST, as it can be confirmed by comparing Fig. 25 with Fig. 23 and Fig. 26 with Fig. 24.

C. DC BUS VOLTAGE EFFECTS

As shown in Figs. 15-18, the currents i_T and i_R, flowing in the transmitting and in the receiving coils, respectively, are substantially sinusoidal, therefore an approximate analysis of the effects of the variation of the HFI dc bus voltage $V_{dc,T}$ can be carried out by considering only their 1st harmonics.

With series-series compensation, at the supply frequency, the total impedances of the two coil-capacitor pairs are ideally equal to zero. Hence, in the transmitting section of the WPTS, there is no 1st harmonic voltage drop across the coil-capacitor series and the 1st harmonic of the HFI output voltage v_{AB} balances the voltage induced by i_R across the transmitting coil. The remaining harmonic components of v_{AB} are applied across the series capacitor. Symmetrically, in the receiving section of the WPTS, the voltage induced across the receiving coil by i_T practically coincides with the 1st harmonic component of the voltage across the rectifier input, whose amplitude is proportional to the rectifier dc bus voltage $V_{dc,R}$.

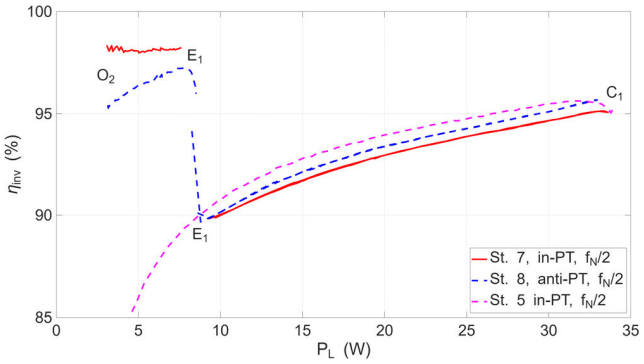

FIGURE 25. Efficiency of the HFI vs. transferred power with Strategy 7 and Strategy 8.

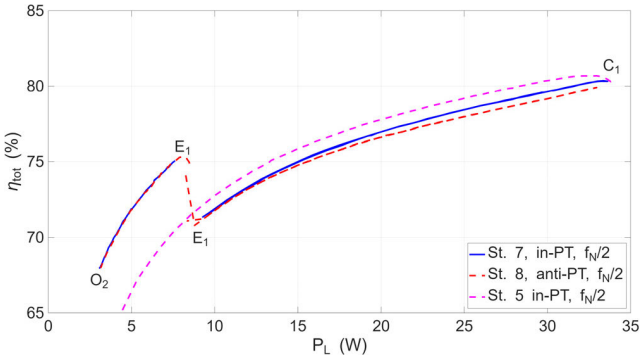

FIGURE 26. Efficiency of the HFI vs. transferred power with Strategy 7 and Strategy 8.

From these two conditions it follows that the variations of v_{AB} mainly influence the amplitude of i_R whilst the amplitude of i_T is mainly influenced by $V_{dc,R}$. Hence, under the hypothesis of 1) increasing $V_{dc,T}$, 2) maintaining $V_{dc,R}$ unchanged, and 3) maintaining δ_A and δ_B unchanged, the amplitude of i_R will increase proportionally to $V_{dc,T}$, the amplitude of i_T will not change, and v_{AB} will increase proportionally to $V_{dc,T}$.

The efficiency η_{inv} and η_{tot} can be expressed by the general equation

$$\eta = \frac{P_{out}}{P_{out} + P_{sw} + P_{cond}}. \tag{34}$$

In the case of the HFI, P_{out} is the power at its output and P_{sw} and P_{cond} are its switching and conduction losses.

The switching losses, which are approximately proportional to $V_{dc,T}$ [24], follow the increase of $V_{dc,T}$ and the same happens to P_{out} if δ_A and δ_B do not change. Instead, the conduction losses, proportional to the square of the amplitude of i_T, do not increase provided that $V_{dc,R}$ is unchanged. Hence, the numerator of (35) increases proportionally to $V_{dc,T}$ whilst, because of P_{cond}, the denominator increases less than proportionally, resulting in an increase of η_{inv}.

If (35) refers to η_{tot}, P_{out} is the power P_L supplied to the load, P_{sw} is the sum of the switching losses of the static converters, and P_{cond} is the sum of the losses that depend on the square of the current amplitudes, i.e. the conduction losses of the static converters and of the coils' windings and the losses of the coils' cores. In this case, P_{cond} increases with $V_{dc,T}$ because of its effect on i_R. The overall effect on η_{tot} cannot be easily assessed because it depends on the relative increase of P_{cond} with respect to P_{out} and P_{sw}.

VIII. CONTROL ALGORITHM FRAMEWORK

The modulation techniques and their implementation in the control strategies described in the previous Subsections must be placed in a broader framework that includes the whole control algorithm involved in the management of the WPTS. The one proposed in [25] can be used as a reference, relating to a bidirectional WPTS used to charge and discharge the battery of an electric vehicle. In this paper only the charging action will be considered.

The WPTS used for the experimental tests detailed in Section V and the one described in [25] are endowed with series-series compensation. As explained in Subsection VII-C, this compensation topology entails that the HFI output voltage v_{AB} acts directly on the receiver coil current, which in turn charges the capacitor C_{DCR} that sustains the dc bus voltage of the receiving section of the WPTS.

According to [25], the controller of the receiving coil current (RCCC) computes the reference $v_{AB,ref}$ for the HFI output voltage processing the receiving coil current reference and feedback. The current reference is generated by the maximum dc voltage regulator (MDCVR) that maintains the voltage across C_{DCR} above a maximum threshold. Finally, the current that charges the battery is limited to the value computed by the minimum dc voltage regulator (mDCVR) that prevents the voltage across C_{DCR} from decreasing below a minimum threshold.

The interaction between the MDCVR and the mDCVR ensures that even if the RCCC fails to impose the secondary coil current, leading to a consequent decrease of the C_{DCR} voltage, the battery charging current is automatically limited or even nullified in order to avoid excessive capacitor discharge. As soon as the C_{DCR} voltage rises again, the battery charging restarts automatically. In this context, the modulation techniques proposed in this paper actuate at the HFI output the voltage reference computed by the RCCC.

As highlighted in Section VI, the different control strategies that can be implemented using the two proposed modulation techniques differ in the maximum voltage they can generate. It is therefore reasonable that the criterion for activating one strategy or the other depends on the value of $v_{AB,ref}$. As an example, the flowchart shown in Fig. 27 can be followed.

In the flowchart, the blocks "Enable Strategy xx" represent the operation of disabling one running strategy to enable another. This operation requires reconfiguring microprocessor peripheral that commands the HFI and generally cannot be performed while the HFI is running. Hence, each strategy change must be performed in five steps: a) gradually decrease the generated voltage to 0, b) disable the HFI, c) change the

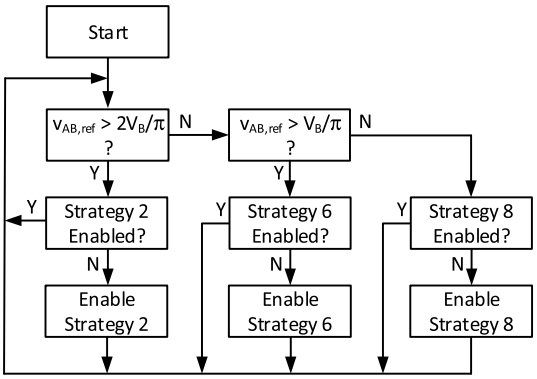

FIGURE 27. Flow chart for the activation of the most suitable control strategy.

microprocessor configuration, d) enable the HFI, e) gradually increase the generated voltage to the required value.

The entire sequence of operations can be completed in a few seconds, so it does not affect the overall battery charging time. Furthermore, considering the interaction between the RCCC, the MDCVR, and the mDCVR algorithms described above, strategy change does not even require modifications to the overall control system to handle the temporary interruption in power transfer.

IX. CONCLUSION

The paper proposed two commutation techniques suitable for the HFI dedicated to supplying the transmitting section of a WPTS. Unlike the PST, the two techniques evenly share the solicitation between the two legs of the HFI and use two control variables to define the output voltage. The harmonic content of the generated voltage has been analyzed as a function of the control variables and some of the obtained results have been represented in the form of maps. Inspection of the maps led to the realization that it is possible to generate the required supply voltage operating the HFI at half of the resonant frequency or commanding only one of its legs, thus significantly increasing its efficiency. The tests carried out on a prototype WPTS confirmed the expected performance of both the proposed modulation techniques from the perspective of the supply voltage commutation and HFI efficiency.

Indeed, it has been demonstrated that both using the anti-PT and the in-PT, in a switching period each of the legs of the HFI is subject to one HVS and one ZVS commutation, instead, using the PST, one leg sustains two HVS commutations whilst the other leg is subject to two ZVS commutations.

By applying Strategy 2, based on the anti-PT operating at f_N, over the whole 0-P_M power range it is possible to obtain a small increase of the overall efficiency ranging from 0.2% to 0.8%. Using Strategy 5 or Strategy 6, which operate at $f_N/2$, the increase of the overall efficiency results between 4% to 10% in the power range 0-$P_M/4$. When the transferred power is lower than $P_M/16$, the overall efficiency can be increased of about 15% operating the HFI at $f_N/2$ and switching only one of its legs, according to Strategy 7 or Strategy 8.

To conclude the paper, a viable approach for the implementation of an overall control algorithm has been provided in the last Section.

REFERENCES

[1] A. Sagar, A. Kashyap, M. A. Nasab, S. Padmanaban, M. Bertoluzzo, A. Kumar, and F. Blaabjerg, "A comprehensive review of the recent development of wireless power transfer technologies for electric vehicle charging systems," *IEEE Access*, vol. 11, pp. 83703–83751, 2023, doi: 10.1109/ACCESS.2023.3300475.

[2] Y. Shanmugam, R. Narayanamoorthi, P. Vishnuram, M. Bajaj, K. M. AboRas, P. Thakur, and Kitmo, "A systematic review of dynamic wireless charging system for electric transportation," *IEEE Access*, vol. 10, pp. 133617–133642, 2022, doi: 10.1109/ACCESS.2022.3227217.

[3] C. Rong, X. Duan, M. Chen, Q. Wang, L. Yan, H. Wang, C. Xia, X. He, Y. Zeng, and Z. Liao, "Critical review of recent development of wireless power transfer technology for unmanned aerial vehicles," *IEEE Access*, vol. 11, pp. 132982–133003, 2023, doi: 10.1109/ACCESS.2023.3332470.

[4] H. Wang, Y. Wu, U. K. Madawala, X. Li, X. Dai, Y. Sun, and J. Hu, "Integrated coupler design for UAV free-positioning wireless power transfer with inherent cross-coupling utilization and enlarged charging coverage," *IEEE Trans. Power Electron.*, vol. 40, no. 10, pp. 14324–14330, Oct. 2025, doi: 10.1109/TPEL.2025.3582935.

[5] A. Wibisono, M. H. Alsharif, H.-K. Song, and B. M. Lee, "A survey on underwater wireless power and data transfer system," *IEEE Access*, vol. 12, pp. 34942–34957, 2024, doi: 10.1109/ACCESS.2024.3373791.

[6] H.-J. Kim, H. Hirayama, S. Kim, K. J. Han, R. Zhang, and J.-W. Choi, "Review of near-field wireless power and communication for biomedical applications," *IEEE Access*, vol. 5, pp. 21264–21285, 2017, doi: 10.1109/ACCESS.2017.2757267.

[7] *Wireless Power Transfer for Light-Duty Plug-in/Electric Vehicles and Alignment Methodology*, Standard SAE J2954_202010, 2020.

[8] R. Pulletikurthi and D. Ronanki, "Review and comparison of modulation schemes for inductive power transfer systems," in *Proc. IEEE Int. Conf. Power Electron., Drives Energy Syst. (PEDES)*, Mangalore, India, Dec. 2024, pp. 1–6, doi: 10.1109/PEDES61459.2024.10961048.

[9] J. Sosa, M. Castilla, L. G. de Vicuna, J. Matas, and J. Miret, "Dynamic analysis and control design of the asymmetrical clamped-mode DC–DC series resonant converter," in *Proc. 32nd Annu. Conf. IEEE Ind. Electron.*, Paris, France, Nov. 2006, pp. 2751–2756, doi: 10.1109/IECON.2006.347650.

[10] J. Zhou, G. Guidi, S. Chen, Y. Tang, and J. A. Suul, "Conditional pulse density modulation for inductive power transfer systems," *IEEE Trans. Power Electron.*, vol. 39, no. 1, pp. 88–93, Jan. 2024, doi: 10.1109/TPEL.2023.3324888.

[11] P. Herasymenko and O. Yurchenko, "An extended pulse-density-modulated series-resonant inverter for induction heating applications," in *Proc. IEEE 61th Int. Sci. Conf. Power Electr. Eng. Riga Tech. Univ. (RTUCON)*, Nov. 2020, pp. 1–8, doi: 10.1109/RTUCON51174.2020.9316617.

[12] J. Tang, T. Na, and Q. Zhang, "A novel full-bridge step density modulation for wireless power transfer systems," *IEEE Trans. Power Electron.*, vol. 38, no. 1, pp. 41–45, Jan. 2023, doi: 10.1109/TPEL.2022.3200759.

[13] W. Zhong and S. Y. R. Hui, "Maximum energy efficiency operation of series-series resonant wireless power transfer systems using on-off keying modulation," *IEEE Trans. Power Electron.*, vol. 33, no. 4, pp. 3595–3603, Apr. 2018, doi: 10.1109/TPEL.2017.2709341.

[14] M. Bertoluzzo, G. Buja, and H. K. Dashora, "Analysis and experimentation of a novel modulation technique for a dual-output WPT inverter," *IEEE Trans. Ind. Electron.*, vol. 70, no. 11, pp. 11174–11184, Nov. 2023, doi: 10.1109/TIE.2022.3227298.

[15] H. Dashora, M. Bertoluzzo, and G. Buja, "Dual-output inverter with phase correction ability for dynamic WPT track supply," in *Proc. 45th Annu. Conf. IEEE Ind. Electron. Soc.*, vol. 1, Lisbon, Portugal, Oct. 2019, pp. 6349–6354, doi: 10.1109/IECON.2019.8927534.

[16] T. Fujita and H. Fujimoto, "Load current control of one pulsewidth modulation for dynamic wireless power transfer system using vehicular AC current estimation," *IEEE J. Emerg. Sel. Topics Ind. Electron.*, vol. 4, no. 3, pp. 939–947, Jul. 2023, doi: 10.1109/JESTIE.2023.3258340.

[17] G. Zhu, J. Dong, W. Shi, T. B. Soeiro, J. Xu, and P. Bauer, "A mode-switching-based phase shift control for optimized efficiency and wide ZVS operations in wireless power transfer systems," *IEEE Trans. Power Electron.*, vol. 38, no. 4, pp. 5561–5575, Apr. 2023, doi: 10.1109/TPEL.2022.3231451.

[18] G. Buja, M. Bertoluzzo, and K. N. Mude, "Design and experimentation of WPT charger for electric city car," *IEEE Trans. Ind. Electron.*, vol. 62, no. 12, pp. 7436–7447, Dec. 2015, doi: 10.1109/TIE.2015.2455524.

[19] L. Yang, S. Jiang, C. Wang, and L. Zhang, "Analysis and design of a CLC/N compensated CC-type WPT system with compact and low-cost receiver," *Sensors*, vol. 23, no. 2, p. 838, Jan. 2023, doi: 10.3390/s23020838.

[20] S. T. Harave, O. Onar, M. Mohammad, V. P. Galigekere, and G.-J. Su, "A novel LCC-CLCC resonant tuning network for light-load conditions in wireless power transfer systems," in *Proc. IEEE Transp. Electrific. Conf. Expo (ITEC)*, Detroit, MI, USA, Jun. 2023, pp. 1–5, doi: 10.1109/ITEC55900.2023.10210328.

[21] J. Yang, X. Zhang, K. Zhang, X. Cui, C. Jiao, and X. Yang, "Design of LCC-S compensation topology and optimization of misalignment tolerance for inductive power transfer," *IEEE Access*, vol. 8, pp. 191309–191318, 2020, doi: 10.1109/ACCESS.2020.3032563.

[22] D.-H. Kim and D. Ahn, "Self-tuning *LCC* inverter using PWM-controlled switched capacitor for inductive wireless power transfer," *IEEE Trans. Ind. Electron.*, vol. 66, no. 5, pp. 3983–3992, May 2019, doi: 10.1109/TIE.2018.2844796.

[23] C. Jiang, K. T. Chau, C. Liu, and C. H. T. Lee, "An overview of resonant circuits for wireless power transfer," *Energies*, vol. 10, no. 7, p. 894, Jun. 2017, doi: 10.3390/en10070894.

[24] D. Graovac, M. Pürschel, and A. Kiep. *MOSFET Power Losses Calculation Using the Data-Sheet Parameters*. Accessed: Oct. 29, 2025. [Online]. Available: https://www.infineon.com/gated/infineon-70-41484-applicationnotes-en_f72138ac-8173-4b5c-8c8e-63dd1e039074

[25] M. Bertoluzzo, A. Kumar, and A. Sagar, "Control strategy for a bidirectional wireless power transfer system with vehicle to home functionality," *IEEE Access*, vol. 11, pp. 60421–60448, 2023, doi: 10.1109/ACCESS.2023.3286302.

MANUELE BERTOLUZZO received the M.S. degree in electronic engineering from the University of Padova, Padua, Italy, in 1993, and the Ph.D. degree in industrial electronics and computer science, in 1997.

Since 2015, he has been an Associate Professor with the Department of Industrial Engineering, University of Padova, and holds the lectureship of road electric vehicles and systems for automation. He is involved in analysis and design of power electronics systems, especially for wireless charging of electric vehicles battery.

NICOLA BIANCHI (Fellow, IEEE) received the M.Sc. and Ph.D. degrees in electrical engineering from the Department of Electrical Engineering, University of Padova, Padua, Italy, in 1991 and 1995, respectively.

In 1998, he joined the Department of Electrical Engineering, University of Padova. Since 2018, he has been a Full Professor in electrical machines, converters and drives. His activity is currently with the Electric Drive Laboratory, Department of Electrical Engineering, University of Padova. His teaching activity deals with the design methods of electrical machines, introducing the finite element analysis of the machines. His research interests include design and control of electrical machines, especially for variable speed applications. He is the author or co-author of more than 250 scientific papers on electrical machines and drives and two international books on the same subject.

Prof. Bianchi is also a member of the Electric Machines Committee and The Electrical Drives Committee of the IEEE Industry Applications Society. In 2014, he became a Fellow Member of IEEE Industry Application Society. He was a recipient of ten best paper awards. He was the Technical Program Chair of the IEEE Energy Conversion Congress and Exposition, in 2014.

FRANCESCO TRIPALDI received the M.S. degree in aerospace engineering from the University of Padova, Italy, in 2023. He is currently working as a Research Fellow with the Electric Drives Laboratory, University of Padova. His research interests include the design of high frequency rotary transformers for the excitation of electrically excited synchronous motors.